nature physics

SUPPLEMENTARY INFORMATION

https://doi.org/10.1038/s41567-018-0225-6

In the format provided by the authors and unedited.

Giant anomalous Nernst effect and quantum-critical scaling in a ferromagnetic semimetal

Akito Sakai[1,2], Yo Pierre Mizuta[3,4], Agustinus Agung Nugroho[1,5], Rombang Sihombing[1,5], Takashi Koretsune[2,4], Michi-To Suzuki[2,4], Nayuta Takemori[4], Rieko Ishii[1], Daisuke Nishio-Hamane[1], Ryotaro Arita[2,4], Pallab Goswami[6,7] and Satoru Nakatsuji[1,2]*

[1]Institute for Solid State Physics, University of Tokyo, Kashiwa, Japan. [2]CREST, Japan Science and Technology Agency (JST), Kawaguchi, Japan. [3]Faculty of Mathematics and Physics, Kanazawa University, Kanazawa, Japan. [4]Center for Emergent Matter Science (CEMS), RIKEN, Hirosawa, Wako, Japan. [5]Faculty of Mathematics and Natural Sciences, Bandung Institute of Technology, Bandung, Indonesia. [6]Condensed Matter Theory Center and Joint Quantum Institute, Department of Physics, University of Maryland, College Park, MD, USA. [7]Department of Physics and Astronomy, Northwestern University, Evanston, IL, USA. *e-mail: satoru@issp.u-tokyo.ac.jp

Supplementary Information

Crystal structure

Co_2MnGa has the cubic ordered full Heusler type structure ($L2_1$) with the space group $Fm\overline{3}m$. It consists of four fcc sublattices with Co atoms at (1/4, 1/4, 1/4) and (3/4,3/4,3/4), Mn atom at (0, 0, 0) and Ga atom at (1/2, 1/2, 1/2). It is known that this structure is prone to have disorder; forming either $B2$ structure with $Pm\overline{3}m$ symmetry, where Mn and Ga atoms are randomly interchanged, or $A2$ structure with $Im\overline{3}m$ symmetry, where all atoms are randomly mixing. Our single crystals were confirmed to have $L2_1$ structure, as clearly represented by the existence of 111 reflections in various diffraction methods: powder X-ray diffraction (XRD) (Fig. S1a), selected area electron diffraction (Fig. S1b) and single crystal XRD. The XRD pattern is well reproduced by the Rietveld analysis as shown by the solid line in Fig. S1a, indicating the single phase of the $L2_1$ cubic Heusler Co_2MnGa with the lattice constant of $a = 5.77(3)$Å (Table S1). To make the powder XRD measurements, we annealed the sample at 700 °C for ~ 3 hours after making powder from single crystals to remove the strains and distortions introduced by the crushing procedure. The 2D- and 1D- characteristic X-ray maps demonstrate the homogeneity of the stoichiometry over the entire sample (Fig. S1c and S1d).

Transport properties and estimation of the transverse thermoelectric conductivity α_{yx}

Figure S2 shows the T dependence of (**a**) the electric resistivity, ρ, (**b**) the Seebeck effect, S_{xx}, and (**c**) thermal conductivity, κ, at zero field, $B = 0$, for each bar-shaped sample labeled by the field

directions applied during the Nernst and Hall effect measurements. Electric and heat current flows along [001] for #100 and #110 and along [10$\bar{1}$] for #111, respectively. All the ρ vs. T curves nearly collapse on top, indicating the small sample dependence and weak anisotropy in ρ. Over one decade between 2 and 40 K, the longitudinal resistivity ρ_{xx} shows T^2 dependence as shown in the inset of Fig. S2a. The solid lines represent the fit to the equation $\rho_{xx} = \rho_0 + AT^2$, which yields $A \sim 8 \times 10^{-4}$ ($\mu\Omega$cm/K^2).

For S_{xx}, only the sample #111 shows different behavior from the other two, indicating the heat current direction dependence of the Seebeck effect. Resistivity monotonically decreases with decreasing T without any minimum, which excludes the possibility of the weak localization effect as discussed in the following section. The small peak in S_{xx} at $\sim$ 90 K can be attributed to the phonon drag since this temperature is close to the typical peak T expected for the phonon drag[1], i.e. $\sim T_{\rm D}/5$ using the Debye temperature $T_{\rm D} = 360 \pm 10$ K estimated in the following section of Supplementary Information.

Similar to the longitudinal resistivity ρ, the thermal conductivity κ also shows small sample dependence and weak anisotropy. $\kappa(T)$ forms a peak around 70 to 90 K most likely following the temperature dependence of the phonon thermal conductivity $\kappa_{\rm ph}$ as often observed in crystalline materials. Namely, assuming the relation $\kappa_{\rm ph} = C_{\rm ph} v l_{\rm ph}/3$, where $C_{\rm ph}$, v and $l_{\rm ph}$ are specific-heat, mean group velocity and mean free path, respectively, it is conceivable that with decreasing T from high temperature, $\kappa_{\rm ph}$ first increases because $l_{\rm ph}$ increases with reducing the phonon-phonon scattering and then peaks with the salutation of $l_{\rm ph}$ and finally decreases roughly proportional to $C_{\rm ph}$ at low Ts.

In general, electric current is generated by both electric field $\vec{E}$ and temperature gradient $\vec{\nabla}T$, namely

$$\vec{J} = \hat{\sigma}\vec{E} - \hat{\alpha}\vec{\nabla}T,$$

where $\vec{J}$, $\hat{\sigma}$ and $\hat{\alpha}$ are the electric current density, the electric and thermoelectric (Peltier) conductivity tensors, respectively. Setting $\vec{B} \parallel \hat{z}$ and $\vec{\nabla}T \parallel \hat{x}$, and the open circuit condition $\vec{J} = 0$, we obtain,

$$J_y \;\; = \;\; \sigma_{yx}S_{xx} + \sigma S_{yx} - \alpha_{yx} = 0,$$

where we assume that the Seebeck coefficient $\sigma = \sigma_{xx} = \sigma_{yy}$ for the cubic symmetry. Using this equation and values from the experiment, we calculate the T dependence of $-\alpha_{yx}$ (Fig. 3b).

Specific heat

Figure S3 shows the temperature dependence of the specific heat divided by T, C/T obtained for Co_2MnGa at zero field. To estimate the Sommerfeld coefficient γ, C/T vs. T^2 below $T \sim 20$ K is plotted in the inset of Fig. S3. The broken line is the fit by $C/T = \gamma + \beta T^2$, where the first and second terms respectively indicate the electronic and low T limit of Debye-type phonon contributions. Using the relation $\beta = (12\pi^4 N k_{\rm B} r)/(5T_{\rm D}^3)$, where N, $k_{\rm B}$, r and $T_{\rm D}$ are the Avogadro's number, Boltzmann constant, number of formula unit per unit-cell and Debye temperature, respectively, we obtain $\gamma = 12.2$ mJ/(moleK^2) and $T_{\rm D} = 366$ K, consistent with the previous report[2]. Experimentally obtained $\gamma = 12.2$ mJ/(moleK^2) is found to be ~ 7 times larger than the value estimated from the first-principles calculation $\gamma = 2$ mJ/(moleK^2). This enhancement should come from the band renormalization due to the strong electron correlation among $3d$ conduction electrons, which is not

taken into account in the first-principles calculation. Namely, this indicates the ~ 7 times shrinkage of the band width in Co_2MnGa than the one obtained from the band calculation. Note that Kadowaki-Woods ratio A/γ^2, where A is the T^2 coefficient of the longitudinal resistivity as discussed in the previous section, can be estimated as $A/\gamma^2 \sim 0.5 \times 10^{-5}$ ($\mu\Omega$cm/K^2)/(mJ/(moleK^2))^2 for Co_2MnGa, which is close to the universal value $A/\gamma^2 \sim 1 \times 10^{-5}$ ($\mu\Omega$cm/K^2)/(mJ/(moleK^2))^2 known for strongly correlated electron systems[3,4].

The solid curve in the main panel of Fig. S3 represents the sum of γT and the specific heat due to Debye phonons, namely.

$$\begin{aligned} C &= \gamma T + C_{\rm D}, \\ C_{\rm D} &= 9Nk_{\rm B}\frac{T^3}{T_{\rm D}^3}\int_0^{T_{\rm D}/T}\frac{x^4e^x}{(e^x-1)^2}dx, \end{aligned}$$

where $\gamma = 12.2$ mJ/(moleK^2) and $T_{\rm D} = 350$ K, which is only slightly smaller than the one obtained from the fitting below 20 K. This fitting well reproduces the specific heat of Co_2MnGa in the wide temperature region, and confirms our low temperature estimates of both electronic and phonon contributions to the specific heat.

Density Functional Theory (DFT) calculation of electronic structure

The electronic structure of Co_2MnGa was obtained by using the QUANTUM ESPRESSO package[5], where the exchange-correlation functional within the generalized-gradient approximation by Perdew-Burke-Ernzerhof[6] and fully-relativistic ultrasoft pseudopotentials were employed. The cutoff energy for the plane wave basis and charge density was set to 100 Ry and 1000 Ry, respectively, and a k-point grid of $18 \times 18 \times 18$ was used.

Following our experimental results given in the first section of Supplementary Information, the lattice constant of Co_2MnGa was set to 5.77 $\mathrm{\AA}$. At the end of self-consistent iterations, the magnetic moment of 4.20 μ_{B}/f.u. was obtained, which is close to the experimentally obtained value ($\sim$ 4.0 μ_{B}) and consistent with the previous calculations based on a full potential method and the expected value from Slater-Pauling rule[7,8].

Fermi surfaces

The Fermi surface of each contributing band is drawn in Fig. S4 in ascending order of energy from left to right. The first three Fermi surfaces are closed around Γ point, which correspond to the hole-like bands near Γ point in Fig. 1b of the main text. The fourth Fermi surface, which is located near the Brillouin zone boundary and the closest to the E_{F}, is the one which we focus on in Fig. 1 (red-colored curves in Figs. 1b-d). The Weyl points shown in Figs. 1c and 1d are formed by the same band as the one constructing this Fermi surface. As discussed in the main text, we believe the proximity to the Weyl points of this Fermi surface is one of the important factors to enhance the anomalous Hall conductivity at E_{F} (Fig. 3e in the main text).

Density of states of Co_2MnGa

The density of states near the Fermi energy is shown in Fig. S5. The broad and sharp peaks observed at $\sim E_{\mathrm{F}}$ and ~ 6 meV above E_{F}, respectively, can contribute to enhance α_{yx} (main text).

Construction of Wannier representation

From the Bloch states obtained in the DFT calculation described above, a Wannier (realistic tight-binding) basis set was constructed using the Wannier90 code[9]. The basis was composed of ($s,\ p,\ d$)- character orbitals localized at each Co and Mn site and ($s,\ p$)- character ones at Ga site, i.e., 62 orbitals/f.u. in total, including spin multiplicity. This set was extracted after iteration for disentangling 116 bands from the space spanned by the original Bloch states in the energy range from -11 eV up to $+50$ eV, while freezing the bands up to $+2$ eV so as to maintain the original dispersion close to the Fermi energy. This iteration was repeated up to the point where the localization of Wannier orbitals improved no more than 0.002% in consecutive steps. No unitary transformation for further localization was performed within the 62 orbitals. Finally, the Wannier-representation of the Hamiltonian was obtained.

Expressions of the anomalous Hall and transverse thermoelectric conductivities

The anomalous Hall conductivity σ_{yx} and the anomalous transverse thermoelectric conductivity α_{yx} that intrinsically appear in crystalline systems can be expressed with the out-of-plane component $\Omega_{n,z}(\mathbf{k})$ of the Berry curvature as follows[10]

$$\sigma_{yx}(T,\ \mu) = -\frac{e^2}{\hbar}\int \frac{d\mathbf{k}}{(2\pi)^3}\Omega_{n,z}(\mathbf{k})f_{n\mathbf{k}}, \tag{S.1}$$

$$\alpha_{yx}(T,\ \mu) = -\frac{e}{T\hbar}\int \frac{d\mathbf{k}}{(2\pi)^3}\Omega_{n,z}(\mathbf{k})\{(\varepsilon_{n\mathbf{k}}-\mu)f_{n\mathbf{k}} + k_{\mathrm{B}}T\log[1+e^{-\beta(\varepsilon_{n\mathbf{k}}-\mu)}]\}, \tag{S.2}$$

where e, $\hbar$, $\varepsilon_{n\mathbf{k}},\ f_{n\mathbf{k}}$, μ are the elementary charge with negative sign, the reduced Planck constant, the band energy, and the Fermi-Dirac distribution function with the band index n and the wave vector $\mathbf{k}$, and μ is the chemical potential. Manipulation of Eq. (S.2) leads to the following simple

relation[10]

$$\alpha_{yx}(T,\ \mu) = \frac{1}{e}\int d\varepsilon \left(-\frac{\partial f}{\partial \varepsilon}\right)\sigma_{yx}(0,\ \varepsilon)\frac{\varepsilon-\mu}{T}, \tag{S.3}$$

which can be approximated as

$$\alpha_{yx}(T,\ \mu \simeq \varepsilon) = -\frac{\pi^2 k_{\mathrm{B}}^2 T}{3\,|e|}\frac{\partial \sigma_{yx}(0,\ \varepsilon)}{\partial \varepsilon} \tag{S.4}$$

at low temperatures where thermal energy broadening is small enough compared to the Fermi energy.

The σ_{yx} and α_{yx} shown in Figs. 3b-d of the main text were computed according to Eqs. (S.1-S.2) in the Wannier representation, using, for the integrations, a k-point mesh of $100 \times 100 \times 100$ and additionally an adaptive mesh of $3 \times 3 \times 3$ in regions with large $\Omega_{n,\ z}$. The α_{yx} shown in Fig. 3e and f of the main text was evaluated by numerical differentiation corresponding to Eq.(S.4).

Weyl point search in the Brillouin zone

The Weyl points, each of them being characterized by a topological charge (Berry flux) of either $\pm 2\pi$ through a closed surface enclosing it, have been searched with our implementation of the method of Fukui-Hatsugai-Suzuki[11]. The search was performed for each one of $50 \times 50 \times 50$ parallelepiped boxes obtained by evenly dividing the Brillouin zone: Evaluating the total Berry flux through the surface of a box, via the computation of overlaps between the Bloch states at neighboring k-points on a 10×10 mesh on each side, it was determined whether the box contains a Weyl point, and if so, which charge it has.

Transverse thermoelectric conductivity $|\alpha_{yx}|$ of various magnets

The values of $|\alpha_{yx}|$ plotted in Fig. 4c in the main text are taken at the temperatures where $|\alpha_{yx}|$ for each magnetic material shows the maximum in its T dependence. Namely, $|\alpha_{yx}| \sim 4$ $\mathrm{AK^{-1}m^{-1}}$ for Co_2MnGa, $|\alpha_{yx}| \sim 1$ $\mathrm{AK^{-1}m^{-1}}$ for MnSi[12], $|\alpha_{yx}| \sim 0.6$ $\mathrm{AK^{-1}m^{-1}}$ for $SrRuO_3$[13], $|\alpha_{yx}| \sim 0.3$ $\mathrm{AK^{-1}m^{-1}}$ for Mn_3Sn[14,15], $|\alpha_{yx}| \sim 0.2$, and 0.12 $\mathrm{AK^{-1}m^{-1}}$ for $La_{1-x}Sr_xCoO_3$ ($x =$ 0.30 and 0.25)[13], $|\alpha_{yx}| \sim 0.03$ $\mathrm{AK^{-1}m^{-1}}$ for $Nd_2Mo_2O_7$[16], $|\alpha_{yx}| \sim 0.25$ and 0.07 $\mathrm{AK^{-1}m^{-1}}$ for $Ga_{1-x}Mn_xAs$ ($x = 0.07$ and 0.05)[17] and $|\alpha_{yx}| \sim 0.0045$ $\mathrm{AK^{-1}m^{-1}}$ for Fe_3O_4[18], from the experimental reports and $|\alpha_{yx}| \sim 0.9, 0.52$ and 0.21 $\mathrm{AK^{-1}m^{-1}}$ for FePt, Co and Fe from the calculations[19]. Normally, the anomalous Nernst effect is seen only in ferromagnets. Note that Fig. 4c includes one exception, the chiral antiferromagnet Mn_3Sn with tiny spontaneous moment $\sim 3\mathrm{m}\mu_\mathrm{B}$/Mn. Interestingly, α_{yx} of Mn_3Sn is comparable to the other ferromagnets[14,15], because the large intrinsic contribution from the Weyl points near E_F [20] dominates the ANE, similarly to the case of Co_2MnGa.

Comment on the positive magnetoconductance

Apart from the chiral anomaly and anisotropic magnetoconductance discussed in the main text, positive longitudinal magnetoconductance (LMC) or negative longitudinal magnetoresistance (LMR) may also arise from other origins such as current jetting effect and weak localization.

In high-mobility compensated semimetals, the transverse magnetoresistance (TMR) can be very large compared to LMR, which is characterized by the large value of the ratio, A=TMR/LMR. For such materials, the current flows directly between the current contacts without spreading along

the perpendicular direction to the field for $\vec{B} \parallel \vec{I}$, hence which is called current jetting[21]. Recently, it has been shown that this current jetting effect is the major origin for the negative LMR observed in several Weyl semimetals[22,23]. In Co_2MnGa, however, the carrier mobility is small compared to the weakly correlated semimetals and zero-gap semiconductors. Moreover, the magnetoresistance is very isotropic $A \sim 1.01$. Nevertheless, we have performed the explicit measurements to rule out the current-jetting effect. Namely, we confirmed that the magnetoconductivity measured at one side (side-A) is almost the same as the one measured at the opposite side (side-B) over the entire range of the magnetic field up to 16 T. We found that this is indeed the case for all the current directions along [100], [110], and [111], as shown in Fig. S6a, S6b, and S6c. Thus, we may conclude that the current jetting effect is negligible in Co_2MnGa.

Moreover, qualitatively the same behaviors, namely the positive magnetoconductance for $\vec{I} \parallel \vec{B}$ and the negative magnetoconductance in high magnetic field for $\vec{B} \perp \vec{I}$, are observed in the measurements with the different current directions such as $\vec{I} \parallel [100]$, $\vec{I} \parallel [110]$ and $\vec{I} \parallel [111]$ as shown in Fig. S6a, S6b, and S6c. For all the current directions, the positive LMC and negative transverse magnetoconductance becomes clear by subtracting the sharp change in magnetoconductance at low fields $B <\sim$0.3 T coming from the magnetic domain reconfiguration (Fig. S6e and S6f). To check the dependence on the angle between $\vec{B}$ and $\vec{I}$, we have carried out the measurements at various angles for the case of $\vec{I} \parallel [111]$ and found that the positive magnetoconductance appears only around $\vec{B} \parallel \vec{I}$, namely $\theta <\sim 10^\circ$) as shown in Fig. S6d. (In the case of $\theta \geq 75^\circ$, a higher field than 9 T is necessary to suppress spin fluctuations (see below) and to induce the negative magnetoconductance, as shown in Fig. S6c). This can be further confirmed by the angle dependence of the magnetoconductance taken at $B = 9$ T (Fig. 4b in the main text). The magne-

toconductance exhibits $\cos^2\theta$ dependence and is indeed positive only when θ is less than 30° for all the cases with $\vec{I} \parallel [100]$, [110] and [111]. These observations provide strong evidence for the chiral anomaly.

To isolate the effect due to the magnetic spin fluctuations, we have carried out the transverse magnetoconductance measurements at various temperatures with $\vec{B} \perp \vec{I} \parallel [100]$. At high temperatures, spin fluctuations are thermally induced and thus dominate the scattering process, while magnetic field may suppress such magnetic scattering. In fact, the positive transverse magnetoconductance is observed at 200 K. However, when we cooled down the system to 100 K, the positive magnetoconductance saturates around 15 T, indicating the crossover to the negative magnetoconductance at $B > 16$ T. With further decreasing temperature down to 5 K, we observe such a crossover appears at 6 T. This confirms that the scattering due to spin fluctuations significantly weakens at low temperatures, and the positive magnetoconductance seen above 6 T for the case of $\vec{B} \parallel \vec{I}$ should not come from spin fluctuations, but from the chiral anomaly.

Field induced suppression of weak localization in conventional dirty semimetals and semiconductors is known to cause the negative magnetoresistance (positive magnetoconductance) in all directions. However, in the absence of magnetic field, weak localization causes the resistivity minimum at low temperatures[24,25]. We do not find such minimum in the temperature dependence of the resistivity for Co_2MnGa (Fig. S2). Therefore, field-induced suppression of weak localization cannot explain the observed magnetoconductance.

Anisotropic magnetoresistance and the proximity to the half metallicity

The half metallicity and its proximity may contribute to the anisotropy in the magnetoresistance and induce so-called anisotropic magnetoresistance (AMR). While Co_2MnGa itself is not a half metal, the proximity is clear from its high spin polarization value $P = 0.6$ revealed by experiment[26]. The AMR for Heusler alloys is extensively studied in thin films and well captured by the recent theory by Kokado $et\ al.$ based on the s-d coupling model[27,28]. The theory predicts that the systematic relation between AMR ratio, $(\rho_{I\|B} - \rho_{I\perp B})/\rho_{I\perp B}$, and valence electron number, $N_{\rm V}$. By using this relation, a positive AMR ratio, namely $\sigma_{I\|B} < \sigma_{I\perp B}$, is expected given $N_{\rm V} \sim 28$ for Co_2MnGa. However, we observe $\sigma_{I\|B} > \sigma_{I\perp B}$ (Fig. S6h), leading to the negative sign of AMR ratio, which contradicts the AMR theory and is consistent with the chiral anomaly.

Effective low energy theory

The expression for anomalous transverse thermoelectric conductivity in Eq. (S.2) can also be written as

$$\alpha_{xy} = \frac{k_B e}{\hbar} \sum_{n,k} \Omega^z_{n,k}\ s_{n,k}, \tag{S.5}$$

where $s_{n,k} = s(\beta[\epsilon_{nk} - \mu]) = -f_{n,k}\ln(f_{n,k}) - (1 - f_{n,k})\ln(1 - f_{n,k})$ is the entropy density for the n th band, and $\beta = 1/(k_B T)$. After introducing an auxiliary variable of integration ϵ, we can rewrite this as

$$\alpha_{xy} = \frac{k_B e}{\hbar} \sum_{n,k} \int d\epsilon\ \Omega^z_{n,k}\delta(\epsilon - \epsilon_{nk})\ s(\beta[\epsilon - \mu]), \tag{S.6}$$

$$= \frac{k_B}{e} \int d\epsilon\ \frac{\partial \sigma_{xy}}{\partial \epsilon}(\epsilon)\ s\left(\frac{\epsilon}{k_B T}\right), \tag{S.7}$$

where the energy derivative of anomalous Hall conductivity σ_{xy} is evaluated at zero temperature.

We are interested in α_{xy} of a tilted, time reversal symmetry breaking Weyl semimetal, for which the right $(+)$ and the left handed $(-)$ Weyl fermions are described by the low energy Hamiltonians,

$$H_{\pm} \approx E_0 \pm \hbar v_2(k_z \mp k_0) + \hbar v_{\perp}(k_x\sigma_x + k_y\sigma_y) \pm \hbar v_1(k_z \mp k_0)\sigma_z. \tag{S.8}$$

In the above equation v_1, v_2 and $v_\perp$ are three independent velocity parameters, and the tilt parameter v_2/v_1 captures the strength of particle-hole anisotropy. For $v_2/v_1 < 1$, we obtain a type I Weyl semimetal with only one of the energy bands (conduction or valence) producing Fermi pockets, while the density of states vanishes at the touching point (located at a reference energy E_0). On the other hand, for $v_2/v_1 > 1$ we find a type II Weyl metal, where both energy bands can produce Fermi pockets, and the electron and hole like pockets touch at the Weyl points. Consequently, the type II Weyl fermions possess a finite density of states at the touching point. These two types of Weyl fermions are separated by the critical tilt parameter $v_2/v_1 = 1$, which corresponds to a quantum Lifshitz critical point.

If the chemical potential remains tuned at the touching points (i.e, $\mu = E_0$), the quantum Lifshitz point describes a phase transition between an incompressible (zero density of states) Weyl semimetal and a compressible Weyl metal. However, the topological properties for any v_2/v_1 remain unaffected, as the coefficients of the three Pauli matrices are kept unchanged. At this critical point, the energy derivative of the anomalous Hall conductivity $\frac{\partial \sigma_{xy}}{\partial \epsilon}(\epsilon)$ shows divergent or singular scaling behavior at low energies. While approaching the critical point, $\xi \sim 1/(k_0|\delta|)$ denotes a divergent correlation length, where $\delta = 1 - v_2/v_1$ is the reduced distance from the critical

point. Therefore, in the vicinity of the Lifshitz point we can write the following scaling form

$$\frac{\partial \sigma_{xy}}{\partial \epsilon}(\epsilon) = \frac{e^2}{4\pi^2 \hbar^2 v_1} F\left(\frac{\epsilon}{|\delta| E_c}\right) \tag{S.9}$$

where, $F(x)$ is a dimensionless scaling function, and $E_c = \hbar v_1 k_0$ is the high-energy cutoff for the low energy theory of Weyl fermions. Consequently, the temperature and chemical potential dependence of α_{xy} can be captured in terms of a scaling function

$$\alpha_{xy}(k_B T, \mu, \delta) = \frac{k_B^2 e T}{4\pi^2 \hbar^2 v_1} G\left(\frac{k_B T}{|\delta| E_c}, \frac{\mu}{|\delta| E_c}\right). \tag{S.10}$$

Through detailed analytical and numerical calculations, we can show that at low energies the energy derivative of the Hall conductivity shows a logarithmic singularity i.e., $\frac{\partial \sigma_{xy}}{\partial \epsilon} \sim \log\left(\frac{|\epsilon|}{\hbar v_1 k_0}\right)$ when $\epsilon \ll \hbar v_1 k_0$. When the system is tuned away from the critical point, this singularity would be rounded off by the finite correlation length, leading to $\frac{\partial \sigma_{xy}}{\partial \epsilon} \sim \log(|\delta|)$ behavior for $\epsilon \ll \delta \hbar v_1 k_0$. Nevertheless in the vicinity of the critical point, the logarithmic singularity manifests itself over a wide range of energies or the quantum critical fan defined as $\delta \hbar v_1 k_0 < \epsilon < \hbar v_1 k_0$. Notably, the logarithmic divergence of $\frac{\partial \sigma_{xy}}{\partial \epsilon}$ at the critical point would lead to $\alpha_{xy} \sim T \log(|E_F - E_0|/(\hbar v_1 k_0))$ behavior at low temperatures. But at high temperatures $k_B T > |E_F - E_0|$, the logarithmic singularity would give rise to $\alpha_{xy} \sim T \log(k_B T/(\hbar v_1 k_0))$ behavior, which captures the quantum critical violation of Mott formula ($\alpha_{xy} \sim T$). We emphasize that the Mott formula will be violated at arbitrarily low temperatures, if the chemical potential is tuned precisely at the touching point ($\mu = E_0$).

The first-principles calculations for Co_2MnGa show the existence of a pair of type-I Weyl fermions with $k_0 \sim 0.15 \times 2\pi/a$ located around $E_0 \approx +0.02$ eV, with a tilt parameter $v_2/v_1 = 0.99$ (Fig. 1 in the main text). These Weyl points are on the verge of undergoing a quantum Lifshitz

transition, with $\delta = 0.01$. Consequently, the characteristic property of a type-I Weyl fermion can only be realized at very low energies when $|E_F - E_0|$ or k_BT are much smaller than $\delta\hbar v_1 k_0 \sim 1$ meV. Since the distance of the Weyl points from the Fermi level $|E_F - E_0| \sim 20$ meV is larger than $\delta\hbar v_1 k_0$, but smaller than $\hbar v_1 k_0 \sim 0.1$ eV, we are actually accessing the quantum critical fan of the Lifshitz point. Therefore, we need to calculate the crossover between $k_BT < \mu$ and $k_BT > \mu$ regimes by essentially restricting ourselves to the quantum critical point.

At the Lifshitz point, the band dispersions along the nodal separation become flat. In particular, one of the bands can produce a very large Fermi pocket along the nodal direction, and it is important to employ a lattice regularization along the nodal separation for avoiding any spurious divergence at large energies or momenta. Hence, we would consider the following approximate two-band model

$$H \approx (E_0 + t_2[\cos(k_z a/2) - \cos(k_0 a/2)])t + v_\perp[k_x\sigma_x + k_y\sigma_y] + t_1[\cos(k_z a/2) - \cos(k_0 a/2)]\sigma_z, \tag{S.11}$$

with $t_1 = t_2 = t$, leading to $v_1 = v_2 = v = ta/(2\hbar)\sin(k_0 a/2)$. For this lattice regularized theory, the scaling functions can be suitably defined as

$$\frac{\partial\sigma_{xy}}{\partial\epsilon} = \frac{e^2}{2\pi^2\hbar ta}\, F\left(\frac{\epsilon}{t}, k_0 a\right), \;\; \alpha_{xy}(k_BT/t, \mu/t) = \frac{k_B^2 eT}{2\pi^2\hbar ta} G\left(\frac{k_BT}{t}, \frac{\mu}{t}\right), \tag{S.12}$$

$$G\left(\frac{k_BT}{t}, \frac{\mu}{t}\right) = \frac{t}{k_BT}\int dx F(x, k_0 a)\; s\left(\frac{t[x - \mu/t]}{k_BT}\right). \tag{S.13}$$

Now we proceed with the evaluation of $F(x, k_0 a)$. For $x > 0$, only the conduction band with energy dispersion $\epsilon_{+,k} = t[\cos(k_z a/2) - \cos(k_0 a/2)] + \sqrt{\hbar^2 v_\perp^2 k_\perp^2 + t^2[\cos(k_z a/2) - \cos(k_0 a/2)]^2}$ can produce a Fermi pocket. In the low energy regime $x = \epsilon/t < 2[1 - \cos(k_0 a/2)]$, the k_z coordinate for the Fermi pocket will be bounded by $\arccos[\cos(k_0 a/2) + x/2] < |k_z a/2| < \pi$.

Therefore, no portion of electron-like pocket would be located in the region $-\arccos[\cos(k_0a/2)+x/2] < k_za/2 < \arccos[\cos(k_0a)+x/2]$. Only in this energy regime, the low energy theory of Weyl fermions can be meaningful. By contrast, for sufficiently large energies satisfying $x > 2[1-\cos(k_0a/2)]$, the electron like pocket would cover the entire length of the Brillouin zone $0 < |k_za| < 2\pi$. Similarly, we can show that for $x < 0$ but $x > -2[1+\cos(k_0a/2)]$, we only obtain a hole pocket in the region $-\arccos[\cos(k_0a/2)+x/2] < k_za/2 < \arccos[\cos(k_0a)+x/2]$. All the integrals for determining F can be performed analytically. However, the actual forms of F are not very illuminating. If we concentrate on $|x| < [1-\cos(k_0a/2)]$,

$$F(x>0,k_0a) = \int_{z_0}^{\pi} dz\ \frac{\cos(z)-\cos(k_0a/2)}{[x+\cos(k_0a/2)-\cos(z)]^2},$$
$$F(x<0,k_0a) = -\int_{0}^{z_0} dz\ \frac{\cos(z)-\cos(k_0a/2)}{[x+\cos(k_0a/2)-\cos(z)]^2},$$

(S.14)

with $z_0 = \arccos[\cos(k_0a/2)+x/2]$. After finishing the integral over z, we find that for small x,

$$F \sim \frac{1}{\sin(k_0a/2)} \log\left(\frac{|\epsilon-E_0|}{C(k_0)\hbar v_1 k_0}\right)$$

as announced in the Eq. (1) of the main text. This logarithmic dependence is clearly identified in the first-principles calculation. After determining F, we can perform the integration over x numerically to obtain α_{xy}, which shows the crossover between the T-linear (at low temperatures $\mu > k_BT$) and $T\log(T/T_0)$ (at high temperatures $k_BT_0 > k_BT > \mu$) behaviors. However, the integrations for $E_F = E_0$, can be done analytically to obtain the results in Eq. (3). By plotting the energy derivative of the anomalous Hall conductivity determined by the first-principles calculation around $E = +0.02$ eV against $\log(E-E_0)$ in Fig. 3f, we establish the $\log(|\epsilon|)$ scaling behavior of the underlying Weyl fermions. Similar logarithmic behaviors are also found

for the other extrema of $\frac{\partial \sigma_{xy}}{\partial \epsilon}$. This indicates the existence of additional pairs of Weyl points which also belong to the quantum critical regime. The contributions of all such pairs can enhance the predictions of effective theory by a factor of N_f, where N_f is the number of such pairs. The experimentally and numerically found $\alpha_{xy}^{\max}$ can be obtained with $N_f \sim 3$. We have also verified that the calculations for the full lattice model only changes the estimation for T_0, but does not cause any significant variation of $\alpha_{xy}^{\max}$.

2. Figure of Merit

For thermoelectric materials based on the Seebeck effect, the dimensionless figure of merit $ZT = \sigma_{xx} S_{xx}^2 T/\kappa_{xx}$ is usually used to estimate the efficiency because the maximum efficiency is described by ZT,

$$\eta_{\rm SE} = \eta_{\rm C} \frac{\sqrt{1+ZT_{\rm av}}-1}{\sqrt{1+ZT_{\rm av}}+T_{\rm c}/T_{\rm h}},$$

where $T_{\rm c}$ and $T_{\rm h}$ are temperatures at the hot and cold parts, $T_{\rm av} = (T_{\rm h}+T_{\rm c})/2$ is the average temperature and $\eta_{\rm C} = (T_{\rm h}-T_{\rm c})/T_{\rm h}$ is Carnot efficiency, respectively [29].

On the other hand, the efficiency for the thermoelectric generation by Nernst effect $\eta_{\rm ANE}$ can be written as

$$\eta_{\rm ANE} = \eta_{\rm C} \frac{1-\sqrt{1-Z_{yx}T_{\rm av}}}{1+\sqrt{1-Z_{yx}T_{\rm av}}},$$

where $Z_{yx}T = \sigma_{xx} S_{yx}^2 T/\kappa_{yy}$ is the figure of merit for ANE [30]. Since the functional form of $\eta_{\rm ANE}$

is very different from that of $\eta_{\rm SE}$, e.g. $\eta_{\rm ANE} \to \eta_{\rm C}$ at $Z_{yx}T \to 1$ while $\eta_{\rm ANE} \to \eta_{\rm C}$ at $ZT \to \infty$, $Z_{yx}T$ cannot be directly compared to ZT.

For Co_2MnGa, we have estimated $Z_{yx}T$ as shown in Fig. S7. $Z_{yx}T$ is nearly isotropic, which is beneficial for applications. $Z_{yx}T$ monotonically increases on heating and reaches $Z_{yx}T \sim 0.08$ (%) at $T = 400$ K. This is much smaller compared to the reported values for Seebeck effect and comparable to those for spin Seebeck effect [31].

1. Ziman, J. M. *Electrons and phonons: the theory of transport phenomena in solids* (Oxford University Press, 1960).

2. Umetsu, R. Y. *et al.* Electronic specific heat coefficient and magnetic properties of L_{21} phase in Co_2YGa (Y = Cr, Mn and Fe) Heusler alloys. *J. Phys.: Conference Series* **200**, 062036 (2010). URL http://stacks.iop.org/1742-6596/200/i=6/a=062036.

3. Kadowaki, K. & Woods, S. Universal relationship of the resistivity and specific heat in heavy-fermion compounds. *Solid State Communications* **58**, 507–509 (1986). URL http://www.sciencedirect.com/science/article/pii/0038109886907854.

4. Tsujii, N., Kontani, H. & Yoshimura, K. Universality in heavy fermion systems with general degeneracy. *Phys. Rev. Lett.* **94**, 057201 (2005). URL https://link.aps.org/doi/10.1103/PhysRevLett.94.057201.

5. Giannozzi, P. *et al.* Quantum espresso: a modular and open-source software project for quantum simulations of materials. *J. Phys.: Cond. Matt.* **21**, 395502 (2009). URL http://stacks.iop.org/0953-8984/21/i=39/a=395502.

6. Perdew, J. P., Burke, K. & Ernzerhof, M. Generalized gradient approximation made simple. *Phys. Rev. Lett.* **77**, 3865–3868 (1996). URL https://link.aps.org/doi/10.1103/PhysRevLett.77.3865.

7. Galanakis, I., Dederichs, P. H. & Papanikolaou, N. Slater-Pauling behavior and origin of the half-metallicity of the full-Heusler alloys. *Phys. Rev. B* **66**, 174429 (2002). URL http://link.aps.org/doi/10.1103/PhysRevB.66.174429.

8. Tung, J.-C. & Guo, G.-Y. High spin polarization of the anomalous Hall current in Co-based Heusler compounds. *New J. Phys.* **15**, 033014 (2013). URL http://stacks.iop.org/1367-2630/15/i=3/a=033014.

9. Mostofi, A. A. *et al.* An updated version of wannier90: A tool for obtaining maximally-localised wannier functions. *Comput. Phys. Commun.* **185**, 2309 – 2310 (2014). URL http://www.sciencedirect.com/science/article/pii/S001046551400157X.

10. Xiao, D., Yao, Y., Fang, Z. & Niu, Q. Berry-phase effect in anomalous thermoelectric transport. *Phys. Rev. Lett.* **97**, 026603 (2006). URL https://link.aps.org/doi/10.1103/PhysRevLett.97.026603.

11. Fukui, T., Hatsugai, Y. & Suzuki, H. Chern numbers in discretized Brillouin zone: Efficient method of computing (spin) Hall conductances. *J. Phys. Soc. Jpn.* **74**, 1674–1677 (2005). URL http://dx.doi.org/10.1143/JPSJ.74.1674.

12. Hirokane, Y., Tomioka, Y., Imai, Y., Maeda, A. & Onose, Y. Longitudinal and transverse thermoelectric transport in MnSi. *Phys. Rev. B* **93**, 014436 (2016). URL https://link.aps.org/doi/10.1103/PhysRevB.93.014436.

13. Miyasato, T. *et al.* Crossover behavior of the anomalous Hall effect and anomalous Nernst effect in itinerant ferromagnets. *Phys. Rev. Lett.* **99**, 086602 (2007). URL http://dx.doi.org/10.1103/PhysRevLett.99.086602.

14. Ikhlas, M. *et al.* Large anomalous Nernst effect at room temperature in a chiral antiferromagnet. *Nature Physics* **13**, 1085–1090 (2017). URL http://dx.doi.org/10.1038/nphys4181.

15. Li, X. *et al.* Anomalous Nernst and Righi-Leduc effects in Mn_3Sn: Berry curvature and entropy flow. *Phys. Rev. Lett.* **119**, 056601 (2017). URL https://link.aps.org/doi/10.1103/PhysRevLett.119.056601.

16. Hanasaki, N. *et al.* Anomalous Nernst effects in pyrochlore molybdates with spin chirality. *Phys. Rev. Lett.* **100**, 106601 (2008). URL https://link.aps.org/doi/10.1103/PhysRevLett.100.106601.

17. Pu, Y., Chiba, D., Matsukura, F., Ohno, H. & Shi, J. Mott relation for anomalous Hall and Nernst effects in $Ga_{1-x}Mn_xAs$ ferromagnetic semiconductors. *Phys. Rev. Lett.* **101**, 117208 (2008). URL https://link.aps.org/doi/10.1103/PhysRevLett.101.117208.

18. Ramos, R. *et al.* Anomalous Nernst effect of Fe_3O_4 single crystal. *Phys. Rev. B* **90**, 054422 (2014). URL https://link.aps.org/doi/10.1103/PhysRevB.90.054422.

19. Weischenberg, J., Freimuth, F., Blügel, S. & Mokrousov, Y. Scattering-independent anomalous Nernst effect in ferromagnets. *Phys. Rev. B* **87**, 060406 (2013). URL https://link.aps.org/doi/10.1103/PhysRevB.87.060406.

20. Kuroda, K. *et al.* Evidence for magnetic magnetic Weyl fermions in a correlated metal. *Nat. Mater.* **16**, 1090–1095 (2017). URL http://www.nature.com/articles/nmat4987.

21. A. B. Pippard, *Magnetoresistance in metals*, volume 2 (Cambridge University Press,1989).

22. Reis, R. D. *et al.* On the search for the chiral anomaly in Weyl semimetals : the negative longitudinal magnetoresistance. *New J. Phys.* **18**, 085006 (2016). URL http://iopscience.iop.org/article/10.1088/1367-2630/18/8/085006/meta.

23. Yuan, Z., Lu, H., Liu, Y., Wang, J. & Jia, S. Large magnetoresistance in compensated semimetals $TaAs_2$ and $NbAs_2$. *Phys. Rev. B* **93**, 184405 (2016). URL https://link.aps.org/doi/10.1103/PhysRevB.93.184405.

24. Hikami, S., Larkin, A. I. & Nagaoka, Y. Spin-orbit interaction and magnetoresistance in the two dimensional random system. *Prog. Theor. Phys.* **63**, 707–710 (1980). URL https://doi.org/10.1143/PTP.63.707.

25. Kawabata, A. Theory of negative magnetoresistance in three-dimensional systems. *Solid State Commun.* **34**, 431–432 (1980). URL http://www.sciencedirect.com/science/article/pii/0038109880906444.

26. Varaprasad, B., Rajanikanth, A., Takahashi, Y. & Hono, K. Highly spin-polarized $Co_2MnGa_{0.5}Sn_{0.5}$ Heusler compound. *Acta Mater.* **57**, 2702 – 2709 (2009). URL http://www.sciencedirect.com/science/article/pii/S1359645409001062.

27. Sakuraba, Y. *et al.* Quantitative analysis of anisotropic magnetoresistance in Co_2MnZ and Co_2FeZ epitaxial thin films: A facile way to investigate spin-polarization in half-metallic Heusler compounds. *Appl. Phys. Lett.* **104**, 172407 (2014). URL http://dx.doi.org/10.1063/1.4874851.

28. Kokado, S., Tsunoda, M., Harigaya, K. & Sakuma, A. Anisotropic magnetoresistance effects in Fe, Co, Ni, Fe_4N, and half-metallic ferromagnet: A systematic analysis. *J. Phys. Soc. Jpn.* **81**, 024705 (2012). URL http://dx.doi.org/10.1143/JPSJ.81.024705.

29. Goldsmid, H. J. Introduction to thermoelectricity. *Berlin, Germany: Springer-Verlag,* (2009).

30. Harman, T. C. & Honig, J. M. Theory of galvano-thermomagnetic energy conversion devices. I. Generators. *J. Appl. Phys.* **33**, 3178–3188 (1962). URL https://doi.org/10.1063/1.1931132. https://doi.org/10.1063/1.1931132.

31. Uchida, K. *et al.* Thermoelectric generation based on spin Seebeck effects. *Proceedings of the IEEE* **104**, 1946–1973 (2016). URL https://doi.org/10.1109/JPROC.2016.2577478.

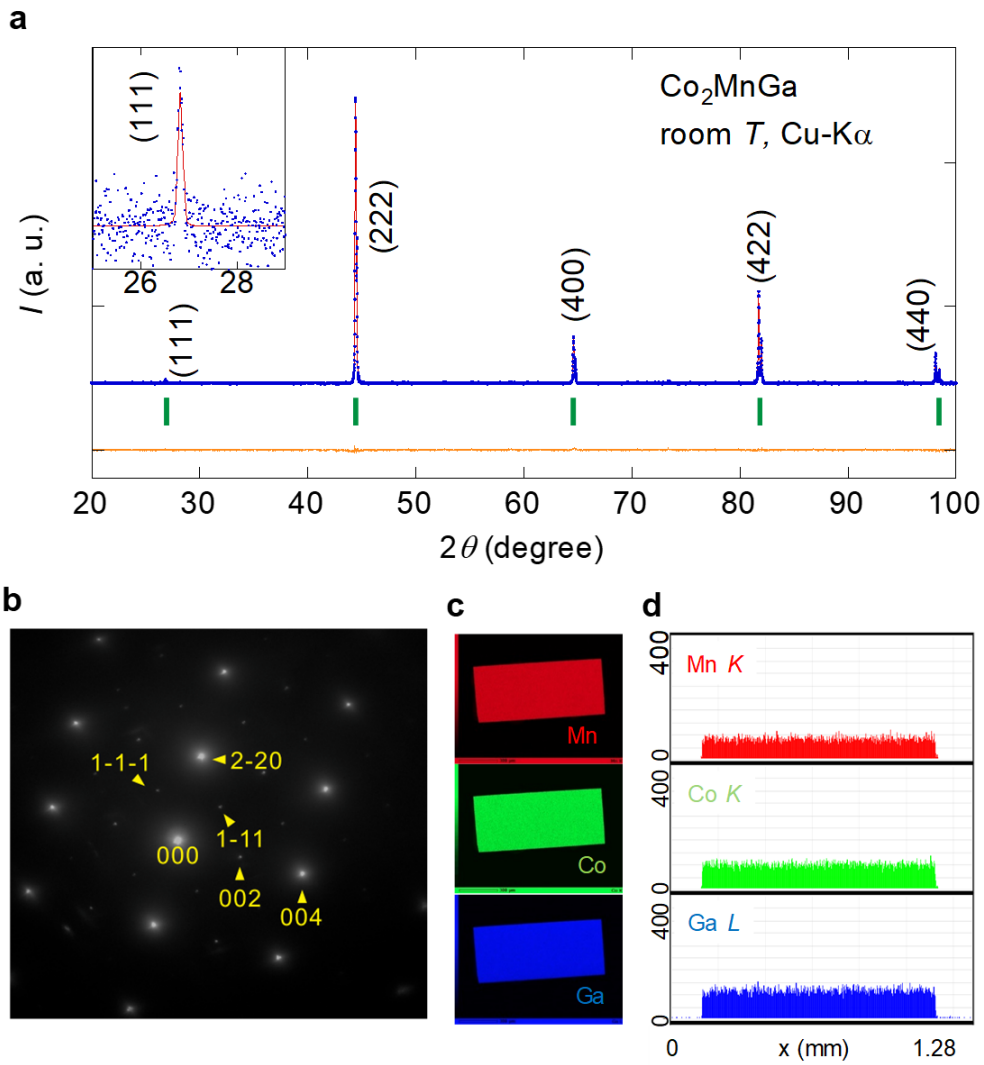

Figure S1 | Evidence for $L2_1$ structure and the homogeneity of the crystal. **a** X-ray diffraction (XRD) pattern of Co_2MnGa obtained by Cu Kα ($\lambda = 1.5401$ Å) radiation at room temperature. The circles and the solid line (red) represent the experimental results and the Rietveld refinement fit, respectively. The final R indicators are $R_{\mathrm{WP}} = 0.69\,\%$, $R_{\mathrm{e}} = 0.65\,\%$ and $S = 1.06$. Vertical bars (green) below the curves indicate the peak positions of the Co_2MnGa full Heusler $L2_1$ phase. The lower curve (orange) represents the difference between the experimental result and the Rietveld refinement. **b** Selected area electron diffraction pattern for our single crystal of

Co_2MnGa along [110]. The reflections of $h + k = 2n$ and $k + l = 2n$ for hkl were observed as the reflections equivalent to [111]. The reflections equivalent to [200] appeared owing to multiple diffraction. **c-d** 2D- (**c**) and 1D- (**d**) X-ray maps of Mn K-, Co K-, and Ga L- lines for the single crystal Co_2MnGa.

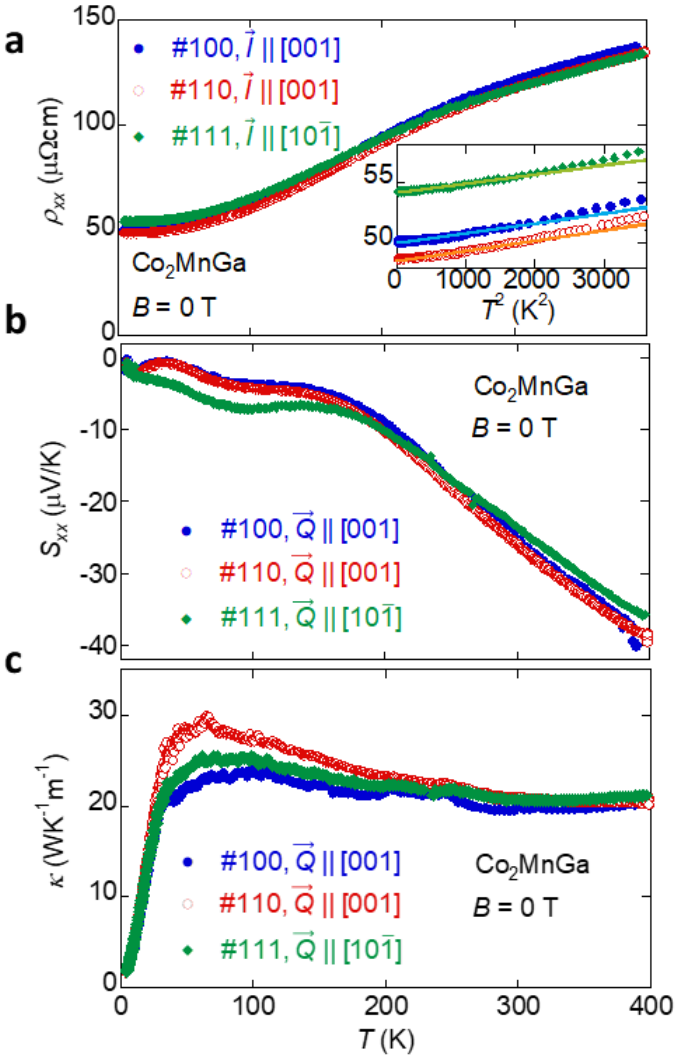

Figure S2 | Electric and thermal transport properties for Co_2MnGa. a-c, Temperature dependence of the longitudinal electric resistivity (**a**), Seebeck effect (**b**) and thermal conductivity κ (**c**) measured at $B = 0$ with different heat current ($\vec{Q}$) directions. Inset of **a** shows T^2 dependence of the longitudinal electric resistivity ρ_{xx}. The solid lines indicate linear fits.

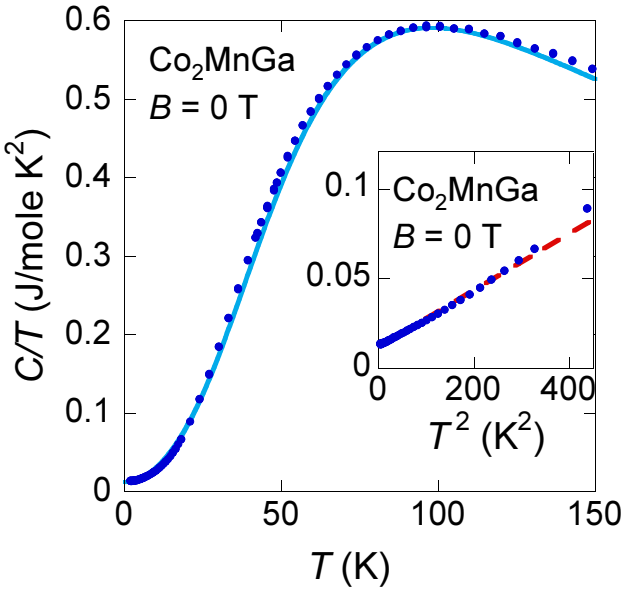

Figure S3 | Specific heat for Co_2MnGa at low temperatures. Temperature dependence of the specific heat divided by T, C/T, for Co_2MnGa measured at $B = 0$ T. The solid curve indicates the fit to the Debye formula. The inset shows the plot of C/T vs. T^2 below $T \sim 20$ K. The broken line indicates a linear fit.

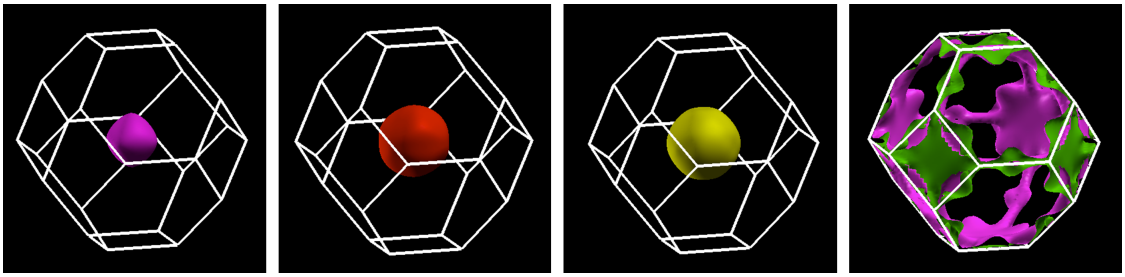

Figure S4 | Fermi surfaces for Co_2MnGa. Fermi surfaces of each band obtained from the first-principles calculation for the case of magnetization of $4.2\mu_B$ along [110] direction (in ascending order of energy).

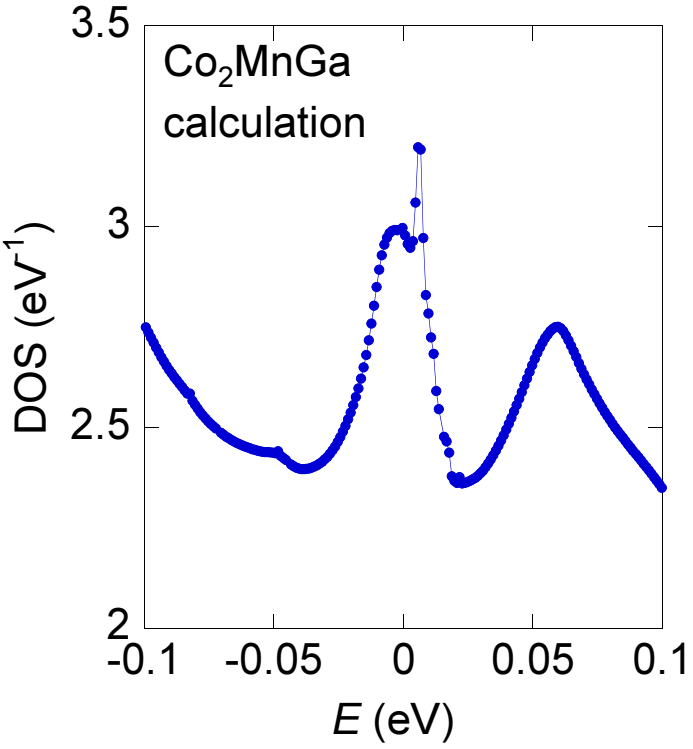

Figure S5 | Density of states for Co_2MnGa obtained from the first-principles calculations. Density of states around the Fermi energy E_F for the case with a magnetization of 4.2 μ_B along [110] direction. A k-point grid of 50×50×50 and an energy smearing of 1 meV were employed.

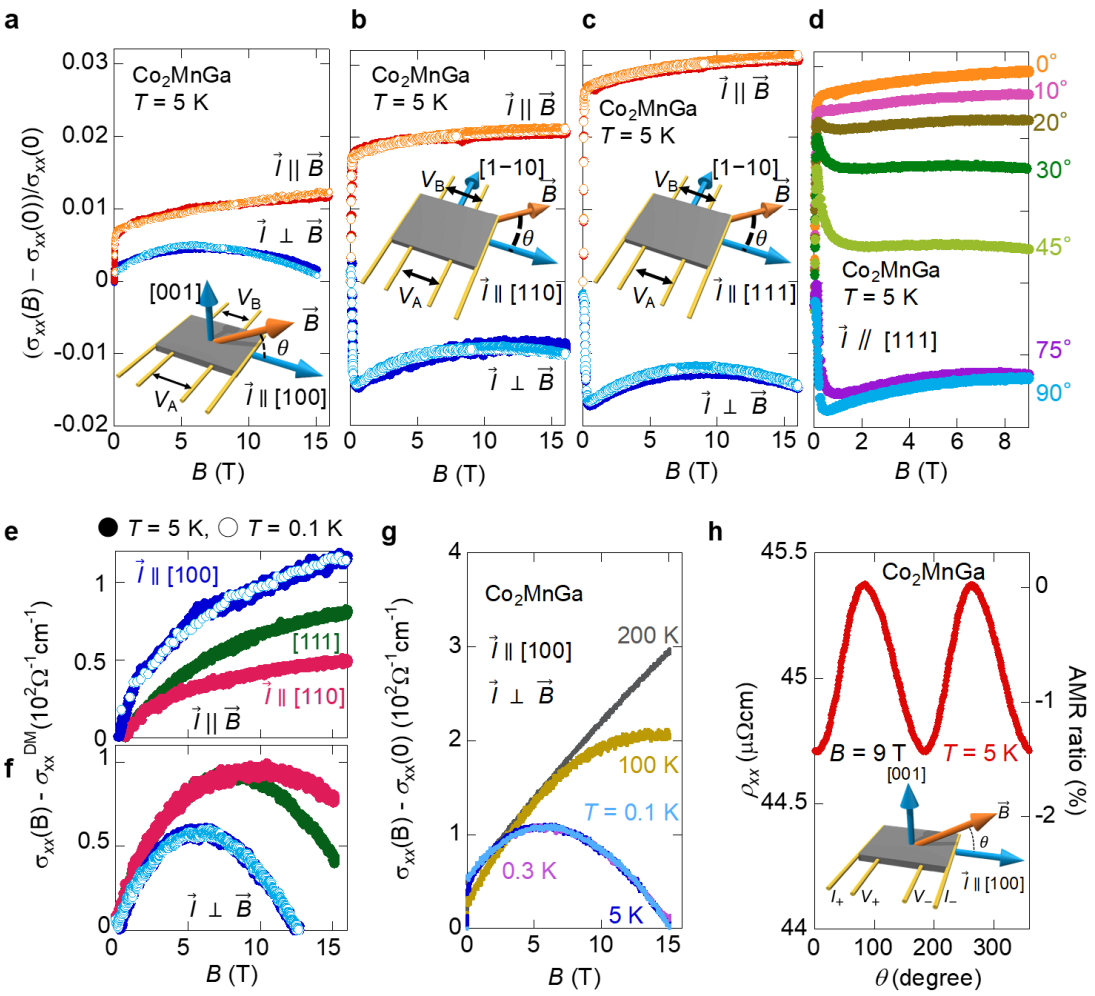

Figure S6 | Absence of the current jetting effect. a-c, Field dependence of the magnetoconductivity $(\sigma_{xx}(B) - \sigma_{xx}(0))/\sigma_{xx}(0)$ measured using the two different voltage terminals on the side-A (solid circles) and the side-B (open circles) for $\vec{I} \parallel [100]$ (**a**), $\vec{I} \parallel [110]$ (**b**) and $\vec{I} \parallel [111]$ (**c**). $\theta = 0$ and 90° correspond to the configurations of $\vec{I} \parallel \vec{B}$ and $\vec{I} \perp \vec{B}$, respectively. The insets show the schematic pictures of the magnetoconductivity measurement set-up to illustrate the voltage V terminal positions at two different sides (side-A and side-B) of a single crystal. Here, θ is the angle between the magnetic field $\vec{B}$ and the electric current $\vec{I}$. **d,** B dependence of the magnetoconductivity at different angles $0° \leq \theta \leq 90°$. **e, f,** B dependence of $\sigma_{xx}(B) - \sigma_{xx}^{\mathrm{DM}}$, where $\sigma_{xx}^{\mathrm{DM}}$ indicates

the magnetoconductivity coming from magnetic domain reconfiguration, measured with $\vec{I} \parallel \vec{B}$ (**e**) and $\vec{I} \perp \vec{B}$ (**f**) and with different current directions, namely, $\vec{I} \parallel$ [100] (blue), $\vec{I} \parallel$ [110] (red) and $\vec{I} \parallel$ [111] (green). **g**, B dependence of $\sigma_{xx}(B) - \sigma_{xx}(0)$ measured at various temperatures for $\vec{I} \parallel$ [100] $\perp \vec{B}$. **h**, Anisotropic magnetoresistance (AMR) ratio of Co_2MnGa as a function of the angle θ at $|\vec{B}| = 9$ T. AMR ratio is defined in the text of Supplementary Information. θ is the angle between the magnetic field and the electric current direction [100], as schematically shown in the inset.

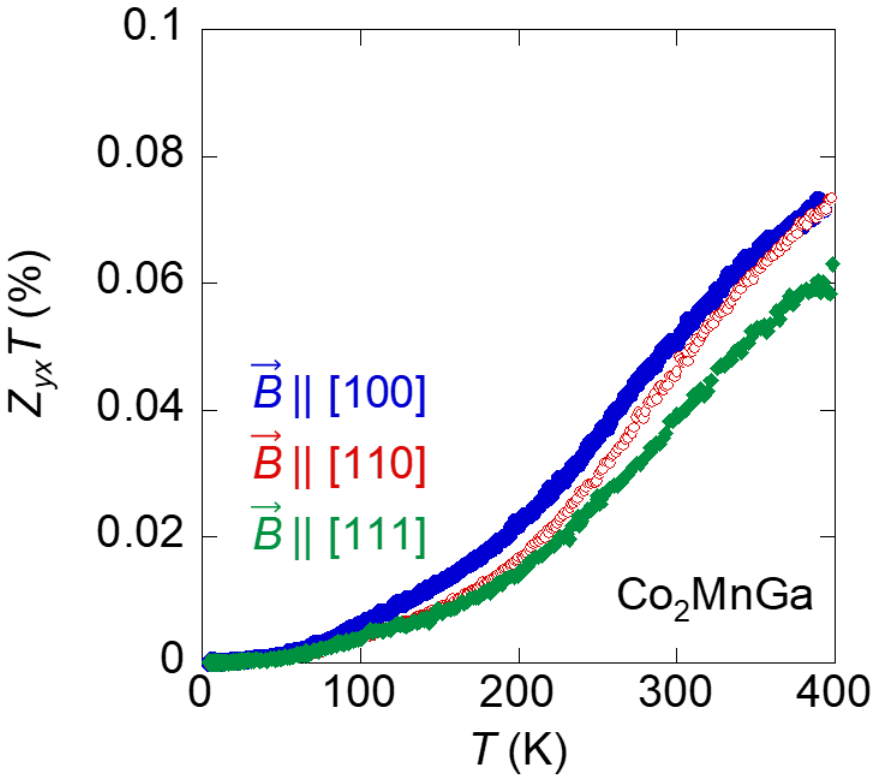

Figure S7| Figure of merit for the Nernst effect of Co_2MnGa. Temperature dependence of the figure of merit $Z_{yx}T$ for the Nernst effect measured in the magnetic field along [100] (blue), [110] (red), and [111] (green) for Co_2MnGa.

Table S1 | Crystal structure parameters for Co_2MnGa at room temperature refined by Rietveld analysis. The lattice parameter is determined by the analysis for the X-ray diffraction spectra with Cu Kα radiation.

lattice parameter 5.77268 Å					
Atom	Wyckoff position	x	y	z	Occupancy
Co	8c	0.25	0.25	0.25	1
Mn	4a	0	0	0	1
Ga	4b	0.5	0.5	0.5	1